nature communications

Article

https://doi.org/10.1038/s41467-025-61130-4

Unraveling the mystery of recent shortened response time of ENSO to Atlantic forcing

Received: 24 October 2024

Accepted: 13 June 2025

Published online: 01 July 2025

Check for updates

Qi Tian[1,2], Jin-Yi Yu[3], Hyacinth C. Nnamchi[4,5], Tim Li[6], Jianping Li[7], Xichen Li[8] & Ruiqiang Ding[1,2]

The El Niño-Southern Oscillation (ENSO) is known to respond to tropical Atlantic (TA) sea surface temperature (SST) forcing. However, the response time of ENSO to the TA SST forcing is not stationary but varies over decades, the reasons for which remain poorly understood. Here we show that decadal changes in ENSO's response time to TA SST forcing are primarily influenced by the south-north shift of the dominant mode of TA SST variability itself. Before the mid-1980s, the southward-shifted TA mode prolongs the response time to ~20 months through an eastward-propagating mid-latitude teleconnection. In contrast, when the TA mode shifts northward after the mid-1980s, the response time decreases to 6–9 months via a faster westward-propagating subtropical teleconnection. Our findings underscore the importance of considering the meridional shift of the TA mode when understanding the impacts of the TA SST variability on ENSO, which has profound implications for ENSO forecasting.

The interactions between the Pacific and Atlantic Oceans have received increasing attention due to their profound impacts on weather and climate[1–4]. El Niño-Southern Oscillation (ENSO), a fluctuation between El Niño and La Niña conditions in the tropical Pacific, can trigger sea surface temperature (SST) variability in the tropical Atlantic (TA) through both tropical and extratropical atmospheric teleconnections[5–11]. In turn, SST variability in the TA, particularly in the North Tropical Atlantic (NTA) and associated with the Atlantic Niño, can also influence the development of ENSO[12–20]. This underscores that the obvious two-way interactions exist between ENSO and the TA SST variability[21–24].

Recent studies have indicated that the influence of the TA SST variability on ENSO can vary markedly over decades[23–34]. In particular, it has been reported that the response time of ENSO to the TA SST forcing has decreased from approximately 20 months before the mid-1980s to around 8 months afterward, likely due to shifts in ENSO frequency from quasi-quadrennial to quasi-biennial patterns[31]. This change suggests that alterations in ENSO characteristics, such as its dominant frequencies[35–37], may play a crucial role in driving the time-varying relationships between ENSO and TA SST variability.

While previous studies suggest that changes in ENSO characteristics explain the shortened response time to TA SST forcing, we propose that alterations in the characteristics of TA SST variability may also play a crucial role in driving the time-varying relationship between ENSO and TA SST variability. We analyze observational data and coupled climate model simulations to investigate this possibility. Our analysis reveals that a northward shift in the dominant mode of TA SST variability, occurring after the mid-1980s, is the primary factor responsible for the reduced response time of ENSO to TA SST variability. This shift highlights that the south-north displacement of the TA SST variability mode can influence ENSO's response time, in addition to the inherent changes in ENSO properties. These findings advance

[1]State Key Laboratory of Earth Surface Processes and Disaster Risk Reduction (ESPDRR), Beijing Normal University, Beijing, China. [2]Key Laboratory of Environmental Change and Natural Disasters of Chinese Ministry of Education, Beijing Normal University, Beijing, China. [3]Department of Earth System Science, University of California, Irvine, California, USA. [4]GEOMAR Helmholtz Centre for Ocean Research Kiel, Kiel, Germany. [5]Department of Geography and Environmental Sustainability, University of Nigeria, Nsukka, Nigeria. [6]Department of Atmospheric Sciences, University of Hawai'i at Manoa, Honolulu, HI, USA. [7]Frontiers Science Center for Deep Ocean Multispheres and Earth System (FDOMES)/Key Laboratory of Physical Oceanography/Institute for Advanced Ocean Studies, Ocean University of China, Qingdao, China. [8]Institute of Atmospheric Physics, Chinese Academy of Sciences, Beijing, China.
e-mail: drq@bnu.edu.cn

our understanding of the inter-basin interactions between the Atlantic and Pacific Oceans and have the potential to contribute to more accurate ENSO predictions.

Results

Decadal changes in the TA – ENSO relationship

We first conducted an empirical orthogonal function (EOF) analysis to extract the dominant modes of monthly SST anomalies in the TA region (30°S–30°N, 70°W–20°E) for the period 1950–2023 (see "Methods"). The first EOF mode features a basin-wide SST anomaly pattern in the TA region, referred to as the TA mode, while the second EOF mode exhibits a meridional dipole SST anomaly pattern relative to the equator (Supplementary Fig. 1), consistent with previous studies[20,38].

We then calculated the 21-year running correlation between the boreal winter (December–February, D^1JF^2, where the superscripts '0', '1', and '2' denote the current year and the following one and two years, respectively) Niño3.4 index and the TA SST index (see Methods) with a lead time of 0–24 months. The results reveal statistically significant negative correlations between the preceding TA SST variability and subsequent ENSO throughout the analysis period. However, the lead time associated with this relationship exhibits considerable decadal change around the mid-1980s (Fig. 1a). Specifically, the TA SST variability can lead ENSO by 18–21 months before the mid-1980s, with the most significant correlation occurring between the boreal spring-to-summer (March–August, $MAMJJA^0$) TA SST and D^1JF^2 Niño3.4 indices (Supplementary Fig. 2). However, this lead time decreased to 6–9 months after the mid-1980s, with the most significant correlation occurring between the $MAMJJA^1$ TA SST and D^1JF^2 Niño3.4 indices. Next, we focus on the TA mode during the spring-to-summer seasons, which coincides with the primary peak seasons of the TA SST variability[20].

Physical mechanisms driving the changes in the TA – ENSO relationship

We next investigated the physical mechanisms responsible for the decadal changes in the TA–ENSO relationship. Notably, the timing of the decadal changes in this relationship coincides with the northward shift of the loading center (see "Methods") of the spring-to-summer TA mode itself (Fig. 1b, c; see also Fig. 1d and Supplementary Fig. 3 for more details). The spatial pattern of the TA mode exhibits the most prominent warming signals in the South Tropical Atlantic (STA) region

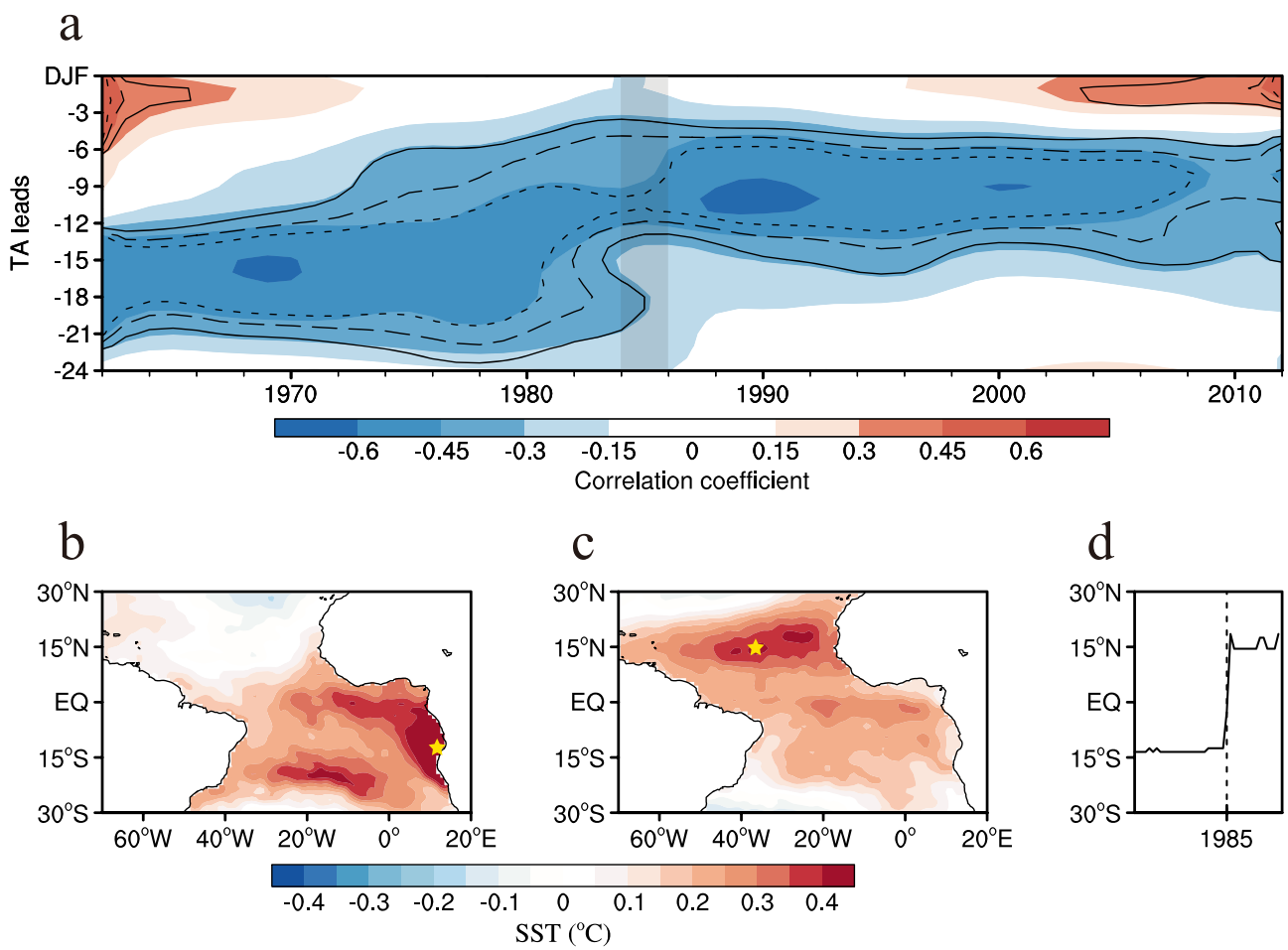

Fig. 1 | Decadal changes in the tropical Atlantic (TA)–El Niño-Southern Oscillation (ENSO) relationship and the south-north shift of the TA mode. a The 21-year running correlation between the boreal winter Niño3.4 index and the TA sea surface temperature (SST) index with a lead time of 0–24 months. Solid, dashed, and dotted lines mark the region with values exceeding the 80, 90, and 95% confidence levels, respectively. The gray vertical bar indicates the approximate timing of the decadal change in the TA–ENSO relationship. **b**, **c** The first empirical orthogonal function (EOF) mode of the boreal spring-to-summer ($MAMJJA^0$) SST (shading; °C) anomalies over the tropical Atlantic during 1960–1984 (P1) (**b**) and 1990–2014 (P2) (**c**). The pentagram denotes the position of the loading center of the TA mode. The impact of the previous winter (D^1JF^0) ENSO signal has been removed from the $MAMJJA^0$ TA SST index using linear regression with respect to the Niño3.4 index. **d** Temporal changes in the latitudinal position of the loading center of the first EOF mode of the $MAMJJA^0$ SST anomalies over the tropical Atlantic during each of the forty 25-year periods.

https://doi.org/10.1038/s41467-025-61130-4

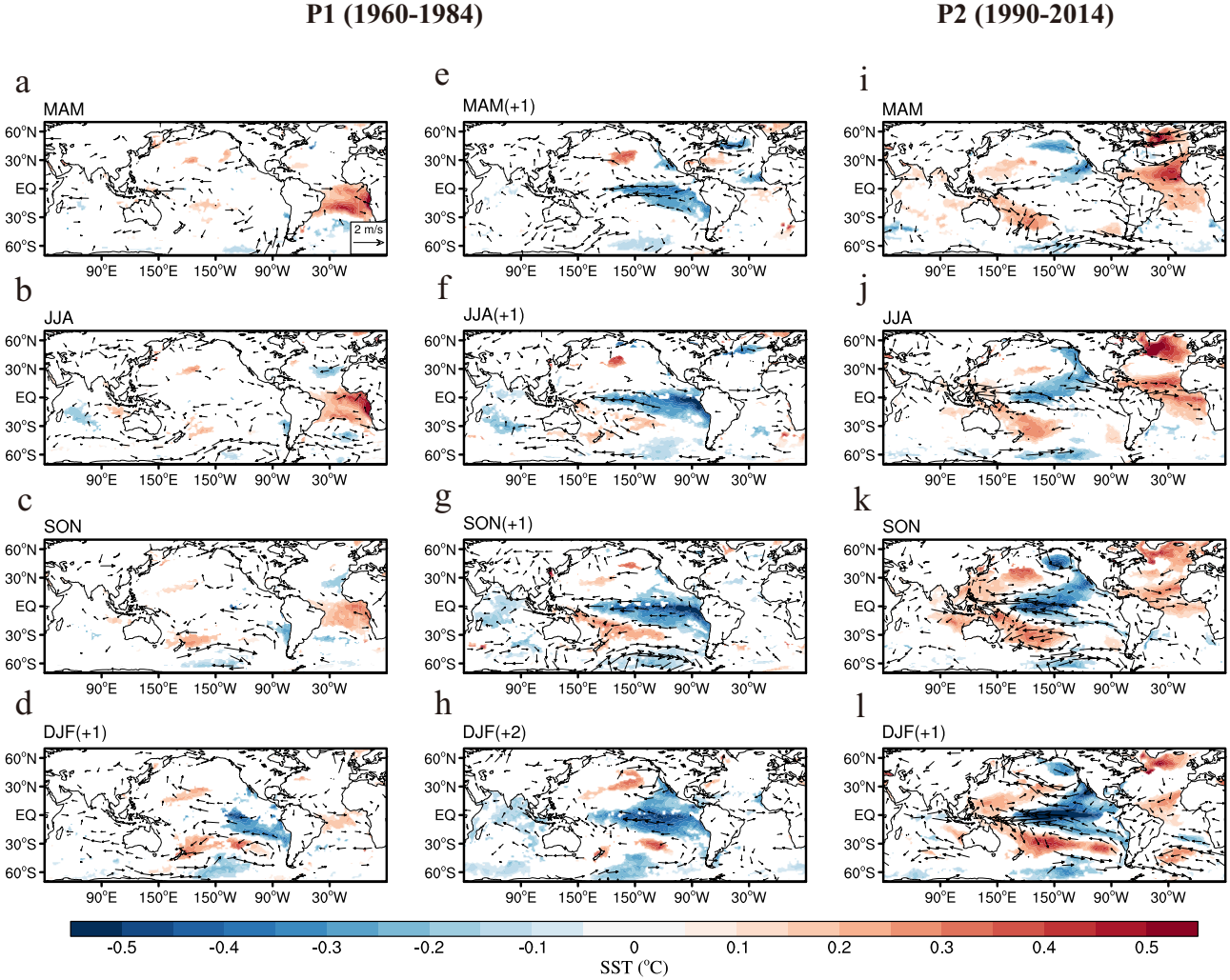

Fig. 2 | Regressions with respect to the spring-to-summer tropical Atlantic (TA) sea surface temperature (SST). a–h Regressions of SST (shading; °C) and 850-hPa winds (vectors; m s^{-1}) with respect to the spring-to-summer (MAMJJA^0, where the superscripts '-1', '0', '1', and '2' denote the previous year, current year, the following one year, and the following two year, respectively) TA SST index during 1960–1984 (P1) for MAM^0 (**a**), JJA^0 (**b**), SON^0 (**c**), D^{0}JF^1 (**d**), MAM^1 (**e**), JJA^1 (**f**), SON^1 (**g**), and D^{1}JF^2 (**h**) seasons. **i–l** As in (**a–d**), but during 1990–2014 (P2) for MAM^0 (**i**), JJA^0 (**j**), SON^0 (**k**), and D^{0}JF^1 (**l**) seasons. The impact of the previous winter (D^{-1}JF^0) El Niño-Southern Oscillation (ENSO) signal has been removed from the MAMJJA^0 TA SST index using linear regression with respect to the Niño3.4 index. Only 850-hPa winds and SST anomalies significant at the 95% confidence level are shown.

for the period 1960–1984 (P1 hereafter) before the mid-1980s, but this pattern shifts northward toward the NTA region for the period 1990–2014 (P2 hereafter) afterward. Furthermore, the correlation patterns between the boreal winter (D^{1}JF^2) Niño3.4 index and the TA SST anomalies with a lead time of 18–21 months show significant negative correlations concentrated in the STA region during P1, but this correlation pattern shifts to the NTA region when the lead time decreased to 6–9 months during P2 (Supplementary Fig. 4). These results suggest that the decadal changes in the TA–ENSO relationship may be attributed to the south-north shift of the TA mode itself.

Note that the northward displacement of the loading center of the TA mode and decadal changes in the TA–ENSO relationship after the mid-1980s may not be manifestations of changes in the decadal SST components of the TA mode. This is because the results from the 11-year high-pass filtered fields resemble those from the unfiltered fields (Supplementary Figs. 5 and 6). Nevertheless, some changes emerge in both the amplitude and large-scale distribution pattern of the TA mode after the removal of low-frequency signals. For instance, upon high-pass filtering, the warming in the STA region weakens prior to the mid-1970s, and the warming in the NTA region also substantially decreases during the period from 1986 to 1995 (Supplementary Figs. 3 and 5). This indicates that low-frequency variability (e.g., the Atlantic Multi-decadal Variability) could also modulate the structure and amplitude of the TA mode[25,39].

A key question that needs to be answered is why the south-to-north shift of the TA mode affects the response time of ENSO to TA SST variability. Previous studies have suggested that NTA SST can influence ENSO through a subtropical teleconnection mechanism[14,15,23,40]. Our analysis indicates that this mechanism is at work during P2, when the loading center of warm SST anomalies in the spring-to-summer TA mode is situated in the NTA region (Fig. 2i–l). As the Atlantic Inter-tropical Convergence Zone (ITCZ) shifts northward toward the NTA region during boreal summer, the MAMJJA^0 NTA warming can efficiently trigger a Gill-type Rossby wave response over the subtropical northeastern Pacific, which in turn generates anomalous anticyclonic flow over the subtropical western Pacific through air-sea coupled interactions. The anticyclonic flow can then enhance the easterly anomaly over the equatorial western Pacific, facilitating the development of a La Niña event in the equatorial Pacific during the subsequent boreal winter (D^{0}JF^1). Therefore, there is a lag of approximately 6–9 months (from MAMJJA^0 to D^{0}JF^1) for the boreal winter ENSO conditions to respond to the preceding spring-to-summer NTA SST

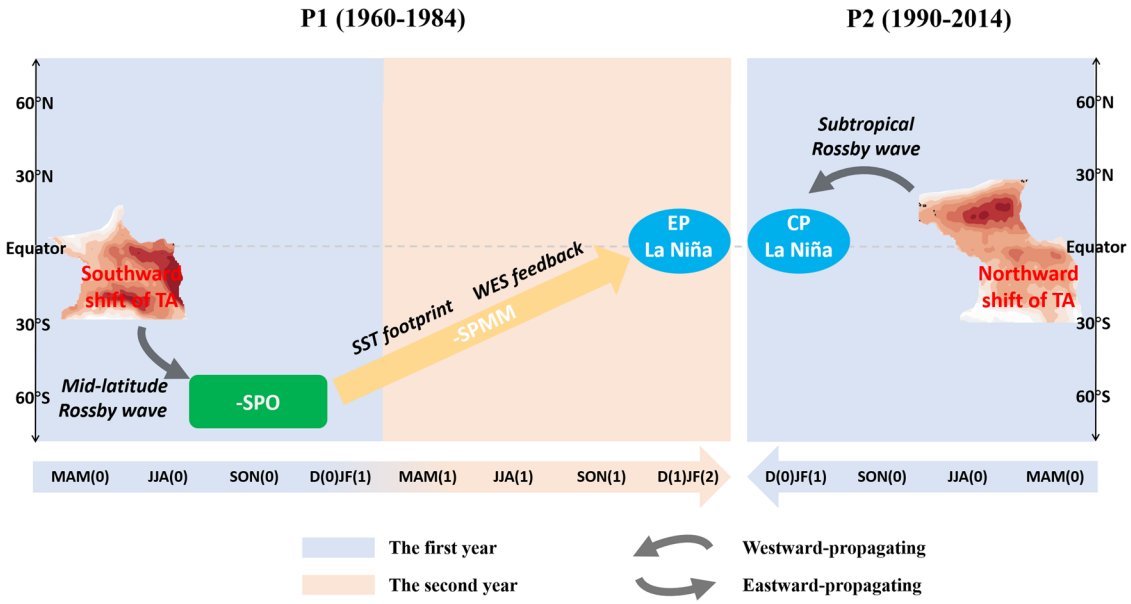

Fig. 3 | Schematic diagram illustrating the physical mechanisms driving the changes in the tropical Atlantic (TA)–El Niño-Southern Oscillation (ENSO) relationship. During 1960–1984 (P1), when spring-to-summer TA mode moves southward, the South Tropical Atlantic (STA) warming can force South Pacific Oscillation (SPO)-like atmospheric circulation anomalies by an eastward-propagating Mid-latitude Rossby wave, which can then induce a South Pacific Meridional Mode (SPMM)-like sea surface temperature (SST) footprint during the winter of the first year. The SPMM interacts with the trade winds and extends negative SST anomalies equatorward into the equatorial Pacific through the wind–evaporation–SST (WES) feedback, leading to an eastern Pacific (EP)-type La Niña event over the equatorial Pacific during the winter of the second year. During 1990–2014 (P2), when spring-to-summer TA mode moves northward, the North Tropical Atlantic (NTA) warming can quickly initiate a central Pacific (CP)-type La Niña event through a westward-propagating subtropical Rossby wave during the winter of the first year.

variability during P2. It should be noted that easterly wind anomalies occur from the Indian Ocean to the western Pacific in boreal summer during P2 (Fig. 2j), which may be attributed to the NTA warming-induced atmospheric Kelvin wave. This aligns with the notion that Kelvin waves can quickly influence subsequent La Niña events[24].

In contrast, a different teleconnection mechanism was active during P1 when the spring-to-summer TA mode exhibited prominent warm SST anomalies in the STA region (Fig. 2a–h). Since the positive heating induced by STA warming is primarily confined to the tropical eastern-central Atlantic (Supplementary Fig. 7a), the Gill-type Rossby wave response cannot extend westward sufficiently to reach the eastern Pacific, unlike the westward influence generated by NTA warming. However, the positive heating from STA warming can excite a stationary Rossby wave train with a barotropic structure propagating eastward in the mid-latitude Southern Hemisphere[41–45] (Supplementary Figs. 7b and 8). The wave activity flux associated with this wave train moves from the South Atlantic southeastward into the southern Indian Ocean, then turns northeastward toward Australia before eventually shifting southeastward into the mid-latitude South Pacific. This process contributes to significant negative South Pacific Oscillation (SPO)-like atmospheric anomalies in that region[46,47] (Fig. 2b, c and Supplementary Fig. 8). It is important to note that STA warming persists from boreal summer into autumn (Fig. 2a–c), further contributing to the sustained SPO anomalies in the South Pacific (Supplementary Fig. 9).

The boreal autumn (OND^0) wind anomalies associated with the SPO can subsequently induce a South Pacific Meridional Mode (SPMM)-like SST anomaly pattern in the subtropical southeastern Pacific during ND^0J^1 by altering surface heat fluxes[46,48,49] (Supplementary Fig. 10). The negative SST anomalies related to the SPMM propagate from subtropics to the central-eastern equatorial Pacific via the wind–evaporation–SST (WES) feedback mechanism, which also intensifies the anomalous easterlies over the equatorial Pacific, further promoting the development of a La Niña event during D^1JF^2 [50–53] (Fig. 2e–h). As a result, the response time of ENSO to STA SST variability is extended during P1, with the entire process spanning approximately 18–21 months (from $MAMJJA^0$ to D^1JF^2).

Here, we schematically summarize the physical mechanisms through which the TA mode modulates the TA–ENSO relationship (Fig. 3). During P1, when the loading center of the $MAMJJA^0$ TA mode shifts southward to the STA region, the STA warming effectively triggers an eastward-propagating Rossby wave train in the mid-latitude Southern Hemisphere, which leads to SPO-like atmospheric anomalies persisting from boreal summer to late autumn (i.e., from JJA^0 to OND^0). The OND^0 SPO then induces a SPMM-like SST footprint during ND^0J^1, which can finally result in a La Niña event during D^1JF^2 (see also Supplementary Fig. 11). In contrast, during P2, when the loading center of the $MAMJJA^0$ TA mode moves northward to the NTA region, along with the northward shift of the Atlantic ITCZ during JJA^0, the NTA warming can quickly initiate a La Niña event during D^0JF^1 via a westward-propagating subtropical Rossby wave. Consequently, the TA–ENSO relationship persists for approximately four seasons longer during P1 compared to P2.

We also note that the northward shift of the SST variability center in the TA mode from P1 to P2 may explain the changes in ENSO types observed over the past few decades[54,55]. During P1, the Pacific SST anomaly pattern induced by STA warming during D^1JF^2 exhibited an eastern Pacific (EP) type of La Niña pattern, with the cooling center primarily located in the eastern equatorial Pacific (Fig. 2h). In contrast, during P2, the NTA warming tends to amplify cooling in the central equatorial Pacific during D^0JF^1, resulting in a central Pacific (CP) type of La Niña pattern (Fig. 2l). These findings suggest that in addition to decadal shifts in the mean state of the tropical Pacific pointed out by previous studie[56–59], the location of the loading center of the TA mode may also influence the diversity of ENSO events[14,15,50,51].

Model verifications

The role of the south-north shift of the TA mode in impacting the response time of ENSO to the TA SST variability is also supported by

https://doi.org/10.1038/s41467-025-61130-4

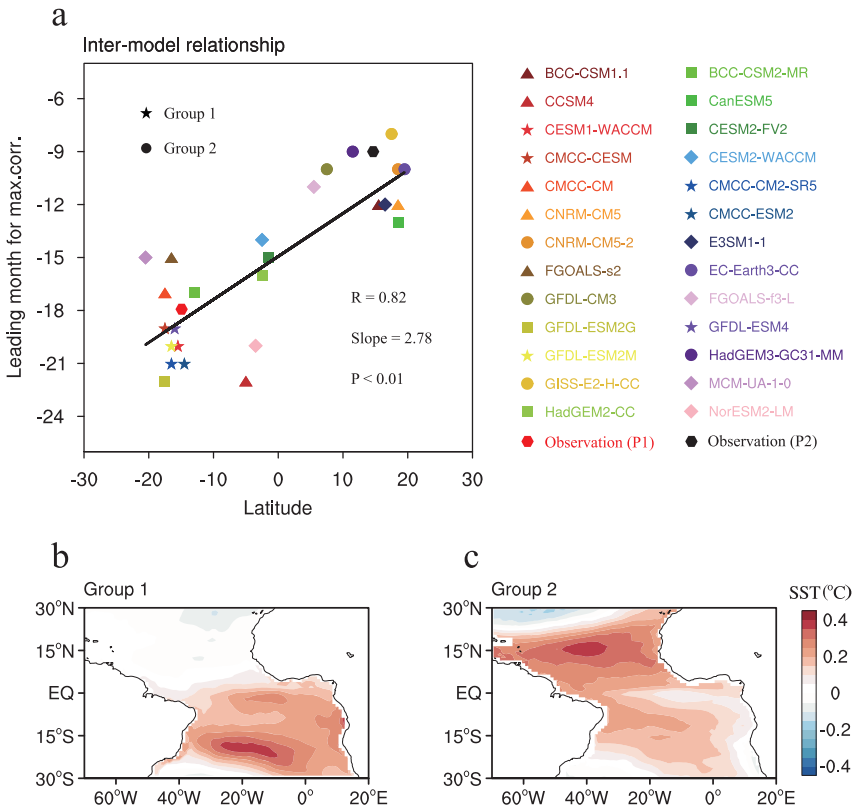

Fig. 4 | Relationship between the locations of the tropical Atlantic (TA) mode and response time of El Niño-Southern Oscillation (ENSO) in the Coupled Model Intercomparison Project (CMIP) historical climate simulations. **a** Scatterplot of the latitudinal positions of the loading center of the TA mode and lead time for which negative correlation coefficients are maximized for the preceding TA sea surface temperature (SST) index with the subsequent winter Niño3.4 index. Here, the latitudinal position of the loading center is obtained as follows: First, the lead time when the negative correlation coefficient between the preceding TA SST index and the subsequent winter Niño3.4 index reaches its maximum is identified. Then, the latitude at which the maximum value of the first empirical orthogonal function (EOF) mode of SST anomalies occurs during this identified lead time is determined. We selected the common analysis period spanning January 1900 to December 1999 for analysis. The linear fit (black solid line) is displayed together with the correlation coefficient R, slope, and *P*-value. The pentagram and circle represent the selected models in Group 1 and Group 2, respectively. The red and black hexagons represent the observations in P1 and P2, respectively. **b**, **c** The first EOF mode of the boreal spring-to-summer ($MAMJJA^0$) SST (shading; °C) anomalies over the tropical Atlantic in Group 1 (**b**) and Group 2 (**c**). The impact of the previous winter ($D^{-1}JF^0$) ENSO signal has been removed from the $MAMJJA^0$ TA SST index using linear regression with respect to the Niño3.4 index.

historical simulations from Coupled Model Intercomparison Project Phase 5 and 6 (CMIP5 and CMIP6) (Supplementary Table 1; see "Methods" for model selections). Among the 26 selected models, there is a high inter-model positive correlation ($R = 0.82$, significant at the 95% confidence level) between the simulated latitudinal positions of the TA mode's loading center and the lead time of the maximum negative correlation between the preceding TA SST index and the following Niño3.4 index (Fig. 4a). This suggests that if the loading center of the TA mode is positioned more northward, the simulated response time of ENSO to TA SST variability would shorten. These findings from coupled climate model simulations provide additional support for our conclusion that the response time of ENSO to TA SST variability is influenced by the south-north shift of the TA mode.

We then divided the models into two groups based on their performance regarding the TA–ENSO relationship: Group 1, which produces a negative TA–ENSO relationship with TA leading ENSO by approximately 18–21 months, and Group 2, where TA leads ENSO by only about 6–9 months. Notably, the loading center of the TA mode in Group 1 is primarily located in the STA region, while in Group 2, it is mainly situated in the NTA region (Fig. 4b, c), aligning with the observational findings. The composited evolutions in the two model groups further support the mechanisms identified in our observational analyses (Supplementary Fig. 12). In Group 1, where the loading center of the spring-to-summer TA mode is positioned further south, the TA SST variability can excite SPO-like atmospheric variability in the South Pacific via an eastward-propagating mid-latitude Rossby wave train, leading to the development of an SPMM during the winter of the first year, which subsequently results in a La Niña event during the winter of the second year. In contrast, in Group 2, the more northward position of the TA mode's SST variability during spring-to-summer can rapidly excite a westward-propagating subtropical Rossby wave, contributing to the development of a La Niña event in the following winter.

Furthermore, we selected 14 models from the 26 pre-selected CMIP5/6 models that simulate well the two types of ENSO events (see "Methods"). We then categorized these 14 models with the loading center of the TA mode located in the STA and NTA regions into Group A and Group B, respectively, and then calculated the winter mean regression values of the Niño4 and Niño3 indices onto the preceding TA SST index for models in Group A and Group B (Supplementary Fig. 13). All 8 models in Group A have regression values for the Niño3 index that are greater than those for the Niño4 index. In contrast, among the 6 models in Group B, 5 models exhibit larger regression values for the Niño4 index compared to the Niño3 index. These results from the models further lend support to the hypothesis that the latitudinal location of the loading center of the TA mode may influence the diversity of ENSO events.

Discussion

We have shown that the south-north shift of the TA mode may be the primary factor of the decadal changes in the TA–ENSO relationship.

Along with the northward movement of the TA mode after the mid-1980s, the response time of ENSO to the TA SST variability is shortened from 18–21 months to 6–9 months. Our results differ from previous studies and attribute this decadal change in the response time to the south-north shift of the TA mode rather than changes in the ENSO cycle[31]. Our findings have profound implications for a better understanding of two-way interactions between the tropical Atlantic and Pacific Oceans and predictions of ENSO.

Our results highlight the impact of the south-north shift of the TA mode on the decadal variability of the TA–ENSO relationship, prompting an investigation into the underlying causes of this shift. We suggest that this displacement may be linked to changes in the intensity of the South Atlantic subtropical high (SASH) and the North Atlantic subtropical high (NASH). Prior to the mid-1980s, the SASH variability was relatively strong, corresponding to the southward shift of the TA mode. In contrast, there has been a marked increase in the strength of the NASH afterward[24,39,60], which aligns with the northward shift of the TA mode (Supplementary Fig. 14a). The possible link between the south-north shift of the TA mode and changes in the NASH/SASH intensity was also supported by the CMIP5/6 model results (Supplementary Fig. 15). It is hypothesized that the increased variability of the NASH and SASH would enhance the northeasterly and southeasterly trade winds, respectively (Supplementary Fig. 14b). This strengthening of the trade winds is likely to amplify the WES feedback, ultimately intensifying the SST anomalies in the NTA and STA regions[61–63]. Hence, fluctuations in the NASH and SASH variability may play a crucial role in the south-north shift of the TA mode.

In addition, notable decadal changes have been observed in the respective magnitudes of the NTA, Atlantic zonal, and STA modes (Supplementary Fig. 16). Specifically, since the mid-1980s, both the STA and Atlantic zonal modes have displayed a weakening trend in magnitude during the spring and summer seasons[64–69]. As a result, relative to the magnitudes of the Atlantic zonal and STA modes, the magnitude of the NTA mode has demonstrated an increasing trend[3,70]. These changes may also have contributed to the south-north shift of the TA mode. Further investigation is necessary to deepen our understanding of this crucial phenomenon.

It is important to note that while we highlight the influence of changes in the TA mode itself on the decadal variability of the TA–ENSO relationship, we do not discount the potential contributions of other processes, such as changes in the ENSO cycle[31]. In addition, considering that there may exist complex nonlinear interactions between changes in the interannual and decadal components of the TA mode, it is hard to disentangle the role of changes in the interannual component of the TA mode from that of changes in its decadal component, or from the interactions between them. We cannot entirely rule out the possibility that the south-north shift of the TA mode and decadal changes in the TA–ENSO relationship after the mid-1980s may also be affected by changes in the background state in the TA region associated with global warming or Atlantic multidecadal oscillation (AMO)[39]. The interactions among these processes and their relative significance require further investigation to attain a comprehensive understanding of the primary factors driving the decadal changes in the TA mode and the TA–ENSO relationship.

Methods

Observed data

We used the monthly mean SST dataset from the Hadley Center Sea Ice and SST dataset version 3 (HadISST; 1871–2023)[71]. Monthly tropospheric winds, geopotential heights, sea level pressure (SLP), precipitation, and wind speed data were derived from NCEP–NCAR Reanalysis 1 (1948–2023)[72]. Our analysis focused on the time period 1950–2023. All of the anomalies are calculated by first removing the average seasonal cycle over the entire period (1950–2023) and then removing the long-term linear trend using the least squares method.

CMIP5/6 historical simulations

We used the monthly historical simulations produced by 50 models taking part in the CMIP5/CMIP6 for the model datasets. From the 50 models, we first selected the 30 models with a significant maximum correlation between the preceding TA SST index and the following Niño3.4 index (Supplementary Fig. 17). Then, given that several climate models (e.g., CSIRO-Mk3.6.0, GISS-E2-R, EC-Earth3-Veg-LR, GFDL-CM4) exhibit considerable changes in the maximum negative correlation between the preceding TA SST index and the subsequent winter Niño3.4 index, we excluded these models and instead selected models in which the maximum negative correlation remains relatively stable over time. Finally, we selected 26 models that meet the aforementioned screening criteria (i.e., temporal stability of the TA SST-Niño3.4 correlation). Supplementary Table 1 provides the main details of the selected models.

Furthermore, we selected 14 models from the 26 pre-selected CMIP5/CMIP6 models for further investigation based on their ability to reproduce the patterns of the CP and EP ENSO in the Taylor diagram and Taylor skill scores[73,74] (Supplementary Fig. 18). To identify the two types of ENSO, we first removed the tropical Pacific SST anomalies that are regressed with the Niño1+2 (0°–10°S, 80°W–90°W) SST index and then applied EOF analysis to the remaining (residual) SST anomalies to obtain the SST anomaly pattern for the CP ENSO[54,55]. Similarly, we subtracted the SST anomalies regressed with the Niño4 (5°S–5°N, 160°E–150°W) index from the total SST anomalies and then applied EOF analysis to identify the leading structure of the EP ENSO.

We selected the mutual time between January 1900 and December 1999 for the analysis. For all the CMIP5 and CMIP6 outputs, the anomalies were obtained on the basis of the full 100-year period. Additionally, all the model data were bilinearly interpolated to a 1° × 1° latitude and longitude grid for multi-model ensemble (MME) mean analysis.

Climate indices

The monthly TA SST index is defined as the principal component (PC) time series associated with the first leading Empirical Orthogonal Function (EOF) of monthly SST anomalies over the TA region (30°S–30°N, 70°W–20°E)[20]. The spring-to-summer (MAMJJA) TA SST index is obtained by calculating the average of the monthly TA SST index from March to August. The Niño3.4 index, the most commonly used index to represent ENSO intensity, is defined as the average of SST anomalies over the Niño3.4 region (5°S–5°N, 170°W–120°W). The SPMM index is obtained by the leading Maximum covariance analysis (MCA) mode of the cross-covariance matrix between SST and 10-m wind anomalies in the subtropical South Pacific (35°–10°S, 180°–70°W). We linearly removed the contemporaneous cold tongue index (CTI; the average SST anomalies between 6°S and 6°N and between 180° and 90°W) from the fields month by month prior to MCA to isolate the local internal variability to exclude the ENSO influence[52]. The SPO index is defined by the first EOF of monthly SLP anomalies in the South Pacific (80°–15°S, 140°E–60°W)[46]. The NASH index is defined as SLP anomalies averaged over the North Atlantic (10°–30°N, 75°W–0°). The SASH index is calculated as SLP anomalies averaged over the South Atlantic (40°–10°S, 50°W–10°E). The Equatorial Atlantic (EA) SST index is defined as SST anomalies averaged over the central-eastern equatorial Atlantic (3°S–3°N, 20°W–0°)[75]. The STA SST index is obtained by SST anomalies averaged over the STA region (30°S–0°, 60°W–10°E). The NTA SST index is defined as SST anomalies averaged over the NTA region (0°–20°N, 90°W–20°E).

The loading center

In this study, the loading center is defined as the latitudinal position where the maximum value of the first EOF mode of SST anomalies is located over the tropical Atlantic.

Rossby wave source and wave activity flux

To explore the influence of the STA warming on the generation of atmospheric Rossby waves, we further analyze the Rossby wave source (RWS)[76] expressed as:

$$S = -\nabla(\mathbf{v}_x\zeta_a) = -fD_x - \zeta D_x - \mathbf{v}_x \cdot \nabla(f+\zeta) \quad (1)$$

where S is the source/sink of the Rossby wave; $\mathbf{v}_x$ represents the divergent wind vector, ζ_a is the absolute vorticity, f and ζ are the planetary vorticity and relative vorticity, respectively, and D_x is the horizontal divergence.

The wave activity flux[77] is used to investigate the stationary Rossby wave propagation induced by the STA warming, which can capture instantaneous wave propagation. Zonal and meridional components of the wave activity flux on the pressure coordinates are calculated according to the following equation:

$$\mathbf{W} = \frac{1}{2|\mathbf{U}|} \times \begin{pmatrix} u\left(\psi_x'^2 - \psi'\psi'_{xx}\right) + v\left(\psi'_x\psi'_y - \psi'\psi'_{xy}\right) \\ u\left(\psi'_x\psi'_y - \psi'\psi'_{xy}\right) + v\left(\psi'^2_y - \psi'\psi'_{yy}\right) \end{pmatrix} \quad (2)$$

where $\mathbf{U} = (u, v)$ is the basic flow, with u and v representing zonal (eastward) and meridional (northward) wind velocity, respectively; ψ is the quasi-geostrophic stream function. Perturbations are denoted by primes, and the subscripts x and y are derivatives in the zonal and meridional direction, respectively.

Significance tests

The statistical significance of the correlations and regressions was determined using a two-tailed Student's t test. To account for the temporal autocorrelation of the time series, the number of effective degrees of freedom was estimated using the method of Bretherton et al.[78]. The significance of linear trends is determined using the Mann–Kendall test, which is a non-parametric test used to detect the presence of linear or non-linear trends in time series.

Data availability

The data that support the findings of this study are freely available. The HadISST dataset is available at http://www.metoffice.gov.uk/hadobs/hadsst3/. The NCEP/NCAR Reanalysis 1 is available at https://psl.noaa.gov/data/gridded/data.ncep.reanalysis.html. The CMIP5 datasets are available at https://esgf-node.llnl.gov/projects/cmip5/. The CMIP6 datasets are available at https://esgf-node.llnl.gov/projects/cmip6/. Source data are provided in this paper.

Code availability

The data in this study were analyzed with the NCAR Command Language (NCL; http://www.ncl.ucar.edu/). All relevant codes used in this study are available, upon request, from the corresponding author R.Q.D.

References

1. McGregor, S. et al. Recent Walker circulation strengthening and Pacific cooling amplified by Atlantic warming. *Nat. Clim. Chang.* **4**, 888–892 (2014).
2. Li, X. C., Xie, S. P., Gille, S. T. & Yoo, C. Atlantic-induced pan-tropical climate change over the past three decades. *Nat. Clim. Chang.* **6**, 275–279 (2016).
3. Cai, W. et al. Pantropical climate interactions. *Science* **363**, eaav4236 (2019).
4. Alexander, M. A. et al. The atmospheric bridge: The influence of ENSO teleconnections on air–sea interaction over the global oceans. *J. Clim.* **15**, 2205–2231 (2002).
5. Enfield, D. B. & Mayer, D. A. Tropical Atlantic sea surface temperature variability and its relation to El Niño-Southern Oscillation. *J. Geophys. Res. Ocean.* **102**, 929–945 (1997).
6. Chiang, J. C. H. & Sobel, A. H. Tropical tropospheric temperature variations caused by ENSO and their influence on the remote tropical climate. *J. Clim.* **15**, 2616–2631 (2002).
7. Chang, P., Fang, Y., Saravanan, R., Ji, L. & Seidel, H. The cause of the fragile relationship between the Pacific El Niño and the Atlantic Niño. *Nature* **443**, 324–328 (2006).
8. McPhaden, M. J., Zebiak, S. E. & Glantz, M. H. ENSO as an Integrating concept in earth science. *Science* **314**, 1740–1745 (2006).
9. Richter, I. et al. Multiple causes of interannual sea surface temperature variability in the equatorial Atlantic Ocean. *Nat. Geosci.* **6**, 43–47 (2013).
10. Taschetto, A. S., Rodrigues, R. R., Meehl, G. A., McGregor, S. & England, M. H. How sensitive are the Pacific–tropical North Atlantic teleconnections to the position and intensity of El Niño-related warming?. *Clim. Dyn.* **46**, 1841–1860 (2016).
11. Jiang, L. & Li, T. Relative roles of El Niño-induced extratropical and tropical forcing in generating Tropical North Atlantic (TNA) SST anomaly. *Clim. Dyn.* **53**, 3791–3804 (2019).
12. Rodríguez-Fonseca, B. et al. Are Atlantic Niños enhancing Pacific ENSO events in recent decades? *Geophys. Res. Lett.* **36**, L20705 (2009).
13. Ding, H., Keenlyside, N. S. & Latif, M. Impact of the equatorial atlantic on the El Niño Southern oscillation. *Clim. Dyn.* **38**, 1965–1972 (2012).
14. Ham, Y. G., Kug, J. S., Park, J. Y. & Jin, F. F. Sea surface temperature in the north tropical Atlantic as a trigger for El Nino/Southern Oscillation events. *Nat. Geosci.* **6**, 112–116 (2013).
15. Ham, Y. G., Kug, J. S. & Park, J. Y. Two distinct roles of Atlantic SSTs in ENSO variability: North Tropical Atlantic SST and Atlantic Nino. *Geophys. Res. Lett.* **40**, 4012–4017 (2013).
16. Keenlyside, N. S., Ding, H. & Latif, M. Potential of equatorial Atlantic variability to enhance El Niño prediction. *Geophys. Res. Lett.* **40**, 2278–2283 (2013).
17. Ham, Y. G. & Kug, J. S. Role of north tropical atlantic SST on the ENSO simulated using CMIP3 and CMIP5 models. *Clim. Dyn.* **45**, 3103–3117 (2015).
18. Martín-Rey, M., Rodríguez-Fonseca, B. & Polo, I. Atlantic opportunities for ENSO prediction. *Geophys. Res. Lett.* **42**, 6802–6810 (2015).
19. Polo, I., Martin-Rey, M., Rodriguez-Fonseca, B., Kucharski, F. & Mechoso, C. R. Processes in the Pacific La Niña onset triggered by the Atlantic Niño. *Clim. Dyn.* **44**, 115–131 (2015).
20. Jiang, L. & Li, T. Impacts of Tropical North Atlantic and equatorial Atlantic SST anomalies on ENSO. *J. Clim.* **34**, 5635–5655 (2021).
21. Wu, L., He, F. & Liu, Z. Coupled ocean-atmosphere response to north tropical Atlantic SST: Tropical Atlantic dipole and ENSO. *Geophys. Res. Lett.* **32**, L21712 (2005).
22. Jansen, M. F., Dommenget, D. & Keenlyside, N. Tropical atmosphere–Ocean interactions in a conceptual framework. *J. Clim.* **22**, 550–567 (2009).
23. Wang, L., Yu, J. Y. & Paek, H. Enhanced biennial variability in the Pacific due to Atlantic capacitor effect. *Nat. Commun.* **8**, 14887 (2017).
24. Park, J.-H. et al. Two regimes of inter-basin interactions between the Atlantic and Pacific Oceans on interannual timescales. *Npj Clim. Atmos. Sci.* **6**, 13 (2023).
25. Martín-Rey, M., Rodríguez-Fonseca, B., Polo, I. & Kucharski, F. On the Atlantic–Pacific Niños connection: a multidecadal modulated mode. *Clim. Dyn.* **43**, 3163–3178 (2014).
26. Kucharski, F. et al. The teleconnection of the tropical Atlantic to Indo-Pacific sea surface temperatures on inter-annual to centennial time scales: A review of recent findings. *Atmosphere* **7**, 29 (2016).
27. Jia, F., Wu, L., Gan, B. & Cai, W. Global warming attenuates the tropical Atlantic-Pacific teleconnection. *Sci. Rep.* **6**, 20078 (2016).

28. Jia, F. et al. Weakening Atlantic Niño–Pacific connection under greenhouse warming. *Sci. Adv.* **5**, eaax4111 (2019).
29. Park, J.-H. & Li, T. Interdecadal modulation of El Niño–tropical North Atlantic teleconnection by the Atlantic multi-decadal oscillation. *Clim. Dyn.* **52**, 5345–5360 (2019).
30. Park, J.-H., Li, T., Yeh, S.-W. & Kim, H. Effect of recent Atlantic warming in strengthening Atlantic–Pacific teleconnection on interannual timescale via enhanced connection with the Pacific meridional mode. *Clim. Dyn.* **53**, 371–387 (2019).
31. Zhang, W., Jiang, F., Stuecker, M. F., Jin, F.-F. & Timmermann, A. Spurious North Tropical Atlantic precursors to El Niño. *Nat. Commun.* **12**, 3096 (2021).
32. Ding, R. et al. North Atlantic oscillation controls multidecadal changes in the North Tropical Atlantic–Pacific connection. *Nat. Commun.* **14**, 862 (2023).
33. Park, J.-H. et al. Distinct decadal modulation of Atlantic-Niño influence on ENSO. *Npj Clim. Atmos. Sci.* **6**, 105 (2023).
34. Zhang, L. et al. Emergence of the central Atlantic Niño. *Sci. Adv.* **9**, eadi5507 (2023).
35. Li, X., Hu, Z. Z., Huang, B. & Jin, F. F. On the interdecadal variation of the warm water volume in the tropical Pacific around 1999/2000. *J. Geophys. Res. Atmos.* **125**, e2020JD033306 (2020).
36. Crespo, L. R., Belén Rodríguez-Fonseca, M., Polo, I., Keenlyside, N. & Dommenget, D. Multidecadal variability of ENSO in a recharge oscillator framework. *Environ. Res. Lett.* **17**, 074008 (2022).
37. Crespo-Miguel, R., Polo, I., Mechoso, C. R., Rodríguez-Fonseca, B. & Cao-García, F. J. ENSO coupling to the equatorial Atlantic: Analysis with an extended improved recharge oscillator model. *Front. Mar. Sci.* **9**, 1001743 (2023).
38. Chiang, J. C. H. & Vimont, D. J. Analogous Pacific and Atlantic meridional modes of tropical atmosphere–Ocean variability. *J. Clim.* **17**, 4143–4158 (2004).
39. Martín-Rey, M., Polo, I., Rodríguez-Fonseca, B., Losada, T. & Lazar, A. Is there evidence of changes in tropical Atlantic variability modes under AMO phases in the observational record?. *J. Clim.* **31**, 515–536 (2018).
40. Ma, J., Xie, S.-P., Xu, H., Zhao, J. & Zhang, L. Cross-basin interactions between the tropical Atlantic and Pacific in the ECMWF hindcasts. *J. Clim.* **34**, 2459–2472 (2021).
41. Li, X., Holland, D. M., Gerber, E. P. & Yoo, C. Impacts of the north and tropical Atlantic Ocean on the Antarctic Peninsula and sea ice. *Nature* **505**, 538–542 (2014).
42. Li, X., Holland, D. M., Gerber, E. P. & Yoo, C. Rossby waves mediate impacts of tropical Oceans on West Antarctic atmospheric circulation in Austral Winter. *J. Clim.* **28**, 8151–8164 (2015).
43. Xue, J. et al. Decadal-scale teleconnection between South Atlantic SST and southeast Australia surface air temperature in austral summer. *Clim. Dyn.* **50**, 2687–2703 (2018).
44. Domeisen, D. I. V., Garfinkel, C. I. & Butler, A. H. The teleconnection of El Niño Southern Oscillation to the stratosphere. *Rev. Geophys.* **57**, 5–47 (2019).
45. Li, X. et al. Tropical teleconnection impacts on Antarctic climate changes. *Nat. Rev. Earth Environ.* **2**, 680–698 (2021).
46. You, Y. & Furtado, J. C. The role of South Pacific atmospheric variability in the development of different types of ENSO. *Geophys. Res. Lett.* **44**, 7438–7446 (2017).
47. Min, Q. & Zhang, R. The contribution of boreal spring South Pacific atmospheric variability to El Niño occurrence. *J. Clim.* **33**, 8301–8313 (2020).
48. Ding, R., Li, J. & Tseng, Y. The impact of South Pacific extratropical forcing on ENSO and comparisons with the North Pacific. *Clim. Dyn.* **44**, 2017–2034 (2015).
49. Li, X., Ding, R., Tseng, Y.-H., Yu, J.-Y. & Xu, X. Mutual influences between ENSO and its two precursor modes in the extratropical South Pacific. *Clim. Dyn.* **62**, 3109–3121 (2024).
50. Zhang, H., Clement, A. & Di Nezio, P. The South Pacific meridional mode: A mechanism for ENSO-like variability. *J. Clim.* **27**, 769–783 (2014).
51. Min, Q., Su, J. & Zhang, R. Impact of the South and North Pacific meridional modes on the El Niño–Southern Oscillation: Observational analysis and comparison. *J. Clim.* **30**, 1705–1720 (2017).
52. You, Y. & Furtado, J. C. The South Pacific Meridional mode and its role in tropical Pacific climate variability. *J. Clim.* **31**, 10141–10163 (2018).
53. Ding, R. et al. On the differences between the South Pacific Meridional and Quadrupole Modes. *J. Geophys. Res. Ocean.* **125**, e2019JC015500 (2020).
54. Kao, H. Y. & Yu, J. Y. Contrasting Eastern-Pacific and Central-Pacific types of ENSO. *J. Clim.* **22**, 615–632 (2009).
55. Kim, S. T. & Yu, J. Y. The two types of ENSO in CMIP5 models. *Geophys. Res. Lett.* **39**, 11704 (2012).
56. Choi, J., An, S. oon-I. l & Yeh, S. W. Decadal amplitude modulation of two types of ENSO and its relationship with the mean state. *Clim. Dyn.* **38**, 2631–2644 (2012).
57. Amaya, D. J. The Pacific Meridional Mode and ENSO: A review. *Curr. Clim. Chang. Rep.* **5**, 296–307 (2019).
58. Feng, Y., Chen, X. & Tung, K. K. ENSO diversity and the recent appearance of Central Pacific ENSO. *Clim. Dyn.* **54**, 413–433 (2020).
59. Capotondi, A. & Ricciardulli, L. The influence of Pacific winds on ENSO diversity. *Sci. Rep.* **11**, 18672 (2021).
60. Lübbecke, J. F., Burls, N. J., Reason, C. J. C. & McPhaden, M. J. Variability in the South Atlantic Anticyclone and the Atlantic Niño Mode. *J. Clim.* **27**, 8135–8150 (2014).
61. Nobre, P. & Shukla, J. Variations of Sea Surface Temperature, Wind Stress, and Rainfall over the Tropical Atlantic and South America. *J. Clim.* **9**, 2464–2479 (1996).
62. Klein, S. A., Soden, B. J. & Lau, N.-C. Remote Sea Surface Temperature Variations during ENSO: Evidence for a Tropical Atmospheric Bridge. *J. Clim.* **12**, 917–932 (1999).
63. Czaja, A., van der Vaart, P. & Marshall, J. A diagnostic study of the role of remote forcing in Tropical Atlantic variability. *J. Clim.* **15**, 3280–3290 (2002).
64. Tokinaga, H. & Xie, S. P. Weakening of the equatorial Atlantic cold tongue over the past six decades. *Nat. Geosci.* **4**, 222–226 (2011).
65. Nnamchi, H. C., Latif, M., Keenlyside, N. S. & Park, W. A Satellite Era warming hole in the equatorial Atlantic Ocean. *J. Geophys. Res. Ocean.* **125**, e2019JC015834 (2020).
66. Prigent, A. et al. Origin of Weakened Interannual Sea Surface Temperature Variability in the Southeastern Tropical Atlantic Ocean. *Geophys. Res. Lett.* **47**, e2020GL089348 (2020).
67. Prigent, A., Lübbecke, J. F., Bayr, T., Latif, M. & Wengel, C. Weakened SST variability in the tropical Atlantic Ocean since 2000. *Clim. Dyn.* **54**, 2731–2744 (2020).
68. Crespo, L. R. et al. Weakening of the Atlantic Niño variability under global warming. *Nat. Clim. Chang.* **12**, 822–827 (2022).
69. Yang, Y. et al. Suppressed Atlantic Niño/Niña variability under greenhouse warming. *Nat. Clim. Chang.* **12**, 814–821 (2022).
70. Yang, Y. et al. Greenhouse warming intensifies north tropical Atlantic climate variability. *Sci. Adv.* **7**, 9690–9715 (2021).
71. Rayner, N. A. et al. Improved analyses of changes and uncertainties in sea surface temperature measured in situ since the mid-nineteenth century: the HadSST2 dataset. *J. Clim.* **19**, 446–469 (2006).
72. Kalnay et al. The NCEP/NCAR 40-year reanalysis project. *Bull. Am. Meteorol. Soc.* **77**, 437–470 (1996).
73. Zhu, H. et al. Does CMIP6 inspire more confidence in simulating climate extremes over China?. *Adv. Atmos. Sci.* **37**, 1119–1132 (2020).

74. Tian, Q., Ding, R. & Li, J. Simulations of the North Tropical Atlantic Mode–ENSO Connection in CMIP5 and CMIP6 Models. *J. Geophys. Res. Atmos.* **128**, e2023JD039018 (2023).
75. Zebiak, S. E. Air–sea interaction in the equatorial Atlantic region. *J. Clim.* **6**, 1567–1586 (1993).
76. Sardeshmukh, P. D. & Hoskins, B. J. The generation of global rotational flow by steady idealized tropical divergence. *J. Atmos. Sci.* **45**, 1228–1251 (1988).
77. Takaya, K. & Nakamura, H. A formulation of a phase-independent wave-activity flux for stationary and migratory quasigeostrophic eddies on a zonally varying basic flow. *J. Atmos. Sci.* **58**, 608–627 (2001).
78. Bretherton, C. S., Widmann, M., Dymnikov, V. P., Wallace, J. M. & Bladé, I. The effective number of spatial degrees of freedom of a time-varying field. *J. Clim.* **12**, 1990–2009 (1999).

Acknowledgements

This research was supported by the National Natural Science Foundation of China (42225501) and the Fundamental Research Funds for the Central Universities (2243300004).

Author contributions

R.Q.D. designed the study. Q.T. and R.Q.D. wrote the paper. Q.T. performed the data analysis and prepared all figures. J.-Y.Y., H.C.N., T.L., J.P.L., and X.C.L. contributed to the interpretation of the results and the improvement of the manuscript.

Competing interests

The authors declare no competing interests.

Additional information

Supplementary information The online version contains supplementary material available at https://doi.org/10.1038/s41467-025-61130-4.

Correspondence and requests for materials should be addressed to Ruiqiang Ding.

Peer review information *Nature Communications* thanks Marta Martín-Rey, and the other anonymous reviewer(s) for their contribution to the peer review of this work. A peer review file is available.

Terms and Conditions

Springer Nature journal content, brought to you courtesy of Springer Nature Customer Service Center GmbH (“Springer Nature”).
Springer Nature supports a reasonable amount of sharing of research papers by authors, subscribers and authorised users (“Users”), for small-scale personal, non-commercial use provided that all copyright, trade and service marks and other proprietary notices are maintained. By accessing, sharing, receiving or otherwise using the Springer Nature journal content you agree to these terms of use (“Terms”). For these purposes, Springer Nature considers academic use (by researchers and students) to be non-commercial.
These Terms are supplementary and will apply in addition to any applicable website terms and conditions, a relevant site licence or a personal subscription. These Terms will prevail over any conflict or ambiguity with regards to the relevant terms, a site licence or a personal subscription (to the extent of the conflict or ambiguity only). For Creative Commons-licensed articles, the terms of the Creative Commons license used will apply.
We collect and use personal data to provide access to the Springer Nature journal content. We may also use these personal data internally within ResearchGate and Springer Nature and as agreed share it, in an anonymised way, for purposes of tracking, analysis and reporting. We will not otherwise disclose your personal data outside the ResearchGate or the Springer Nature group of companies unless we have your permission as detailed in the Privacy Policy.
While Users may use the Springer Nature journal content for small scale, personal non-commercial use, it is important to note that Users may not:

1. use such content for the purpose of providing other users with access on a regular or large scale basis or as a means to circumvent access control;
2. use such content where to do so would be considered a criminal or statutory offence in any jurisdiction, or gives rise to civil liability, or is otherwise unlawful;
3. falsely or misleadingly imply or suggest endorsement, approval , sponsorship, or association unless explicitly agreed to by Springer Nature in writing;
4. use bots or other automated methods to access the content or redirect messages
5. override any security feature or exclusionary protocol; or
6. share the content in order to create substitute for Springer Nature products or services or a systematic database of Springer Nature journal content.

In line with the restriction against commercial use, Springer Nature does not permit the creation of a product or service that creates revenue, royalties, rent or income from our content or its inclusion as part of a paid for service or for other commercial gain. Springer Nature journal content cannot be used for inter-library loans and librarians may not upload Springer Nature journal content on a large scale into their, or any other, institutional repository.
These terms of use are reviewed regularly and may be amended at any time. Springer Nature is not obligated to publish any information or content on this website and may remove it or features or functionality at our sole discretion, at any time with or without notice. Springer Nature may revoke this licence to you at any time and remove access to any copies of the Springer Nature journal content which have been saved.
To the fullest extent permitted by law, Springer Nature makes no warranties, representations or guarantees to Users, either express or implied with respect to the Springer nature journal content and all parties disclaim and waive any implied warranties or warranties imposed by law, including merchantability or fitness for any particular purpose.
Please note that these rights do not automatically extend to content, data or other material published by Springer Nature that may be licensed from third parties.
If you would like to use or distribute our Springer Nature journal content to a wider audience or on a regular basis or in any other manner not expressly permitted by these Terms, please contact Springer Nature at

onlineservice@springernature.com